OPEN ACCESS
IOP Publishing
Journal of Optics
J. Opt. 19 (2017) 114006 (8pp)
https://doi.org/10.1088/2040-8986/aa8d56

Silicon photonic processor of two-qubit entangling quantum logic

R Santagati[1,7,8], J W Silverstone[1,7,8], M J Strain[2,3], M Sorel[2], S Miki[4], T Yamashita[4], M Fujiwara[5], M Sasaki[5], H Terai[4], M G Tanner[2,6], C M Natarajan[2], R H Hadfield[2], J L O'Brien[1] and M G Thompson[1]

[1] Quantum Engineering Technology Labs, H. H. Wills Physics Laboratory and Department of Electrical and Electronic Engineering, University of Bristol, BS8 1FD, United Kingdom
[2] School of Engineering, University of Glasgow, Glasgow G12 8QQ, United Kingdom
[3] Institute of Photonics, SUPA Department of Physics, University of Strathclyde, Technology and Innovation Centre, 99 George Street, G1 1RD, Glasgow, United Kingdom
[4] National Institute of Information and Communications Technology, 588-2 Iwaoka, Kobe 651-2492, Japan
[5] National Institute of Information and Communications Technology, 4-2-1 Nukui-Kitamachi, Koganei, Tokyo 184-8795, Japan
[6] Heriot-Watt University and University of Edinburgh, Queens Medical Research Institute, University of Edinburgh, EH16 4TJ, Edinburgh, United Kingdom

E-mail: raffaele.santagati@bris.ac.uk and josh.silverstone@bris.ac.uk

Received 30 June 2017, revised 5 September 2017
Accepted for publication 18 September 2017
Published 17 October 2017

Abstract

Entanglement is a fundamental property of quantum mechanics, and is a primary resource in quantum information systems. Its manipulation remains a central challenge in the development of quantum technology. In this work, we demonstrate a device which can generate, manipulate, and analyse two-qubit entangled states, using miniature and mass-manufacturable silicon photonics. By combining four photon-pair sources with a reconfigurable six-mode interferometer, embedding a switchable entangling gate, we generate two-qubit entangled states, manipulate their entanglement, and analyse them, all in the same silicon chip. Using quantum state tomography, we show how our source can produce a range of entangled and separable states, and how our switchable controlled-Z gate operates on them, entangling them or making them separable depending on its configuration.

Keywords: silicon quantum photonics, integrated quantum information processing, entanglement, photonic qubits, quantum photonics

(Some figures may appear in colour only in the online journal)

1. Introduction

Photons remain a promising vehicle for the development of next-generation quantum technology [1, 2]. Integrated quantum photonics, with its intrinsic phase stability and miniature devices, is necessary to bring linear optics to the large scale [3–5]. Several integrated photonic platforms have emerged to solve this problem, including silica-on-silicon [3, 6–8], direct-write glass [9–13], lithium niobate [14–17], silicon nitride [18, 19] and silicon-on-insulator [20]. Silicon quantum photonics promises to simultaneously achieve the required functionality, performance, and scale.

Several important quantum optical functionalities have already been shown with high performance in silicon. Photon pairs can be generated using spontaneous four-wave mixing (SFWM) [21–26], and interfered with high visibility [26–30]. Single-photon [31] and pump-rejection [32, 33] spectral demultiplexers, as well as two-mode interferometers [34], have been

[7] These authors contributed equally to this work.
[8] Authors to whom any correspondence should be addressed.

Original content from this work may be used under the terms of the Creative Commons Attribution 3.0 licence. Any further distribution of this work must maintain attribution to the author(s) and the title of the work, journal citation and DOI.

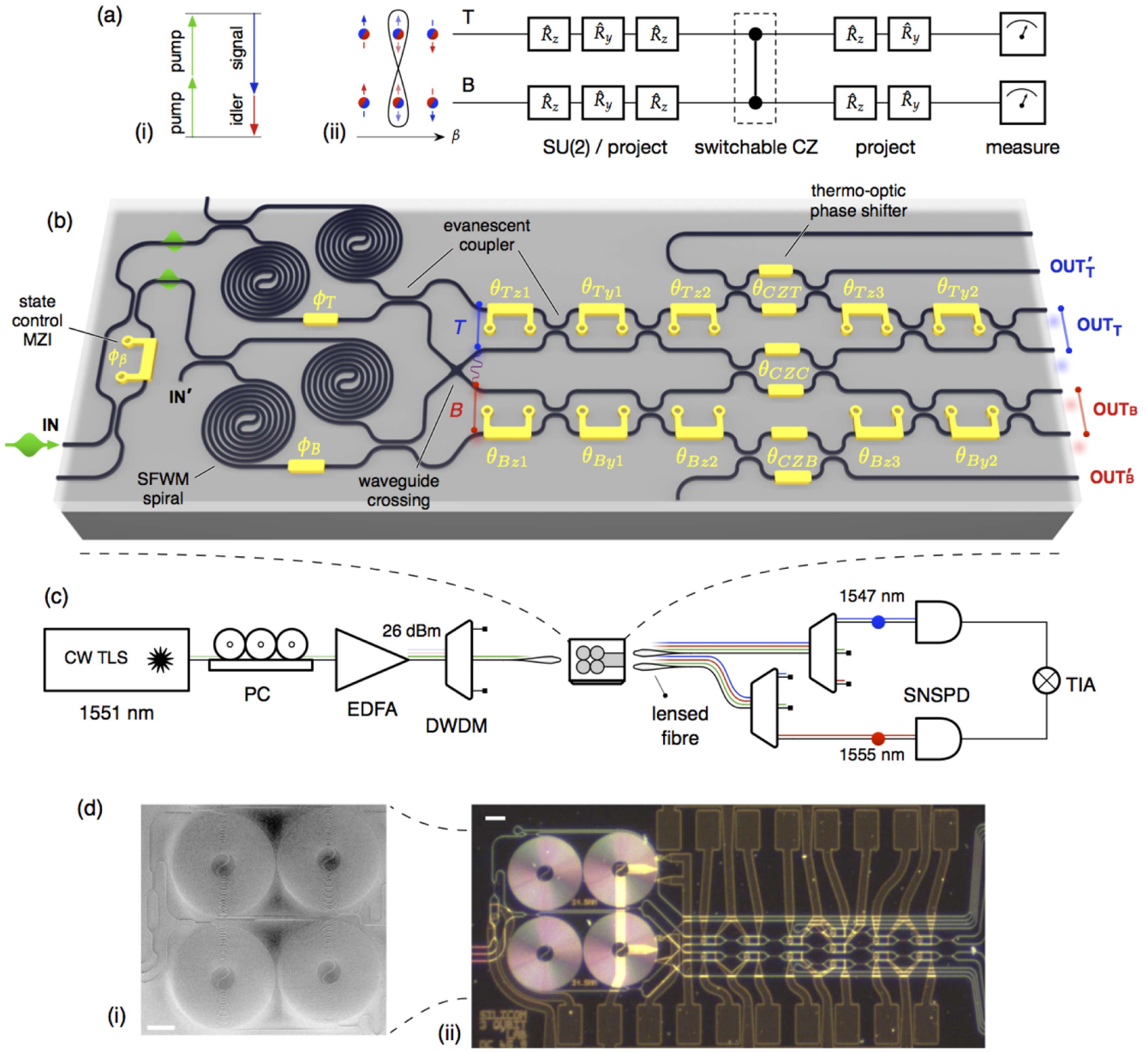

Figure 1. Device and apparatus overview. (a) Operating principles. (i) Non-degenerate spontaneous four-wave mixing, (ii) quantum circuit description. (b) Schematic of the silicon quantum photonic chip. A pump laser is coupled into the device, coherently pumping two spiralled RHOM sources which produce two photons entangled or separable in path. These are fed into a reconfigurable linear optical network which can entangle or disentangle them, and analyse the output. (c) Off-chip apparatus. A continuous wave (CW) tunable laser source (TLS) is polarisation controlled (PC), amplified (EDFA), filtered and coupled onto the chip using lensed fibres and spot-size converters. Signal, idler, and pump photons coupled back into fibre in the same way, then spatially separated using dense wavelength-division multiplexers (DWDM), detected using superconducting nanowire single-photon detectors (SNSPD), and the output signal is analysed by a time interval analyser (TIA). (d) Electron (i) and optical (ii) micrographs of the device.

demonstrated with very high extinction. Finally, single-photon detectors, based on superconducting nanowires have shown excellent performance on silicon waveguides [35, 36]. The very high refractive index contrast of silicon-on-insulator waveguides yields micron-scale components (e.g. [37]), while miniature ring resonator SFWM sources [22], and quantum interferometric networks [38] facilitate devices on a very large scale.

The integration of entangled qubit sources with entangling quantum logic, together on a common platform, is an important next step. Here, we show a new method for generating path-encoded, variably entangled two-qubit states. We perform multi-qubit quantum logic on these states and study their entanglement. We implemented this scheme on a reconfigurable, silicon photonic device to generate a wide range of two-qubit states. We integrated this source with arbitrary state preparation, a switchable two-qubit gate, and an interferometer for tomographic analysis. The implemented quantum circuit is similar to the one reported in [39].

We tested the device's quantum logic capabilities with several experiments. We analysed the source performance using reversed-Hong–Ou–Mandel-type (RHOM) [28, 40] quantum interference, and qubit tomography on a wide range

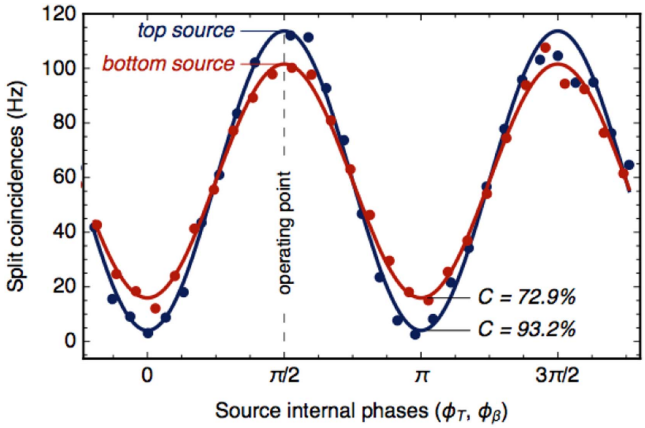

Figure 2. Quantum interference for the two sources, measuring coincidences from the outputs OUT'_T and OUT'_B, obtained by pumping each RHOM source and scanning the source internal phase, ϕ_T or ϕ_B. The imperfect interference can be explained in terms of imbalance in the on-chip evanescent coupler beam splitters.

of possible states. We followed this with an exploration of the on-chip quantum logic, with the switchable two-qubit gate in both entangling ($\hat{cz}$) and non-entangling ($\hat{I}$) configurations, and using the purity (P) [41], the CHSH parameter (S) [42] and the Schmidt number (K) [43] as diagnostic metrics.

2. Device structure and operation

A schematic of the device is shown in figure 1(a). It comprises a reconfigurable source of two path-encoded entangled photons, controlled by the parameters ϕ_β, ϕ_T and ϕ_B. The source is followed by a reconfigurable interferometer, able to implement any two-qubit projector (including entangled projections). This second part of the device can be divided into three sections: arbitrary single qubit gates, a switchable post-selected controlled-Z (cz) gate [44], and final single-qubit unitaries, used to implement projectors for quantum state tomography, to reconstruct the output state.

The device comprised $500 \times 220\,\mathrm{nm}^2$ waveguides, directional couplers (approximate length 45.9 μm), a waveguide crossing (>20 dB isolation), and resistive metallic heaters (length 54.0 μm). It was coupled to fibre via edge coupling, fibre lenses, and polymer spot-size converters. Electrical connections were achieved through multi-contact electrical probes and 200 μm pitch on-chip gold pads (approximately $120 \times 200\,\mu\mathrm{m}^2$). Fabrication of the device proceeded as in [31].

The experimental setup is presented in figure 1(b). Photons are generated on the chip via SFWM, pumped by an amplified continuous-wave tunable laser, and filtered to remove in-band noise. An average facet-to-facet transmission of ≈ -28 dB was observed. The dominant sources of loss were scattering at the chip facets, and propagation loss in the spiralled source waveguides. Inside the device the light was reconfigurably manipulated by an interferometric network, composed of evanescent coupler beam-splitters and thermo-optic phase-shifters [38, 45]. Photons were collected from the

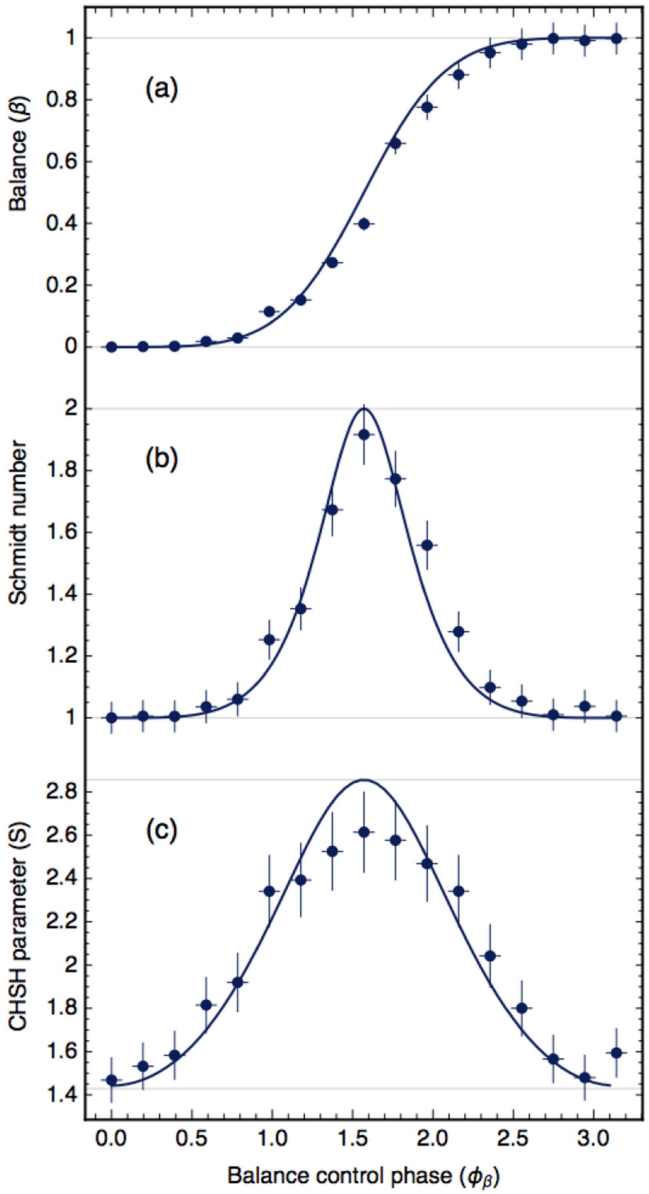

Figure 3. Two-qubit state properties, direct from the source, as a function of the input state control phase, ϕ_β. (a) Balance between the $|00\rangle$ and the $|11\rangle$ components of the state, see equation (2). (b) Schmidt number. (c) CHSH parameter. Maximal entanglement occurs when the state is balanced, when $\phi_\beta = \pi/2$. Error bars were computed as one standard deviation of 200 trials around each tomographic measurement, each with a random sampling of Poisson photon noise. We assume a control phase uncertainty of $\pm\pi/50$.

device, demultiplexed and separated from the pump using dense wavelength-division multiplexers, detected using superconducting nanowire detectors [46], and finally converted into coincidence counts by a time-interval analyser.

2.1. Photon-pair generation

The strong nonlinear properties of silicon waveguides are well known [47]. SFWM, an effect of the $\chi^{(3)}$ nonlinearity, is now commonly used to produce photon pairs in silicon quantum photonic devices [21, 28].

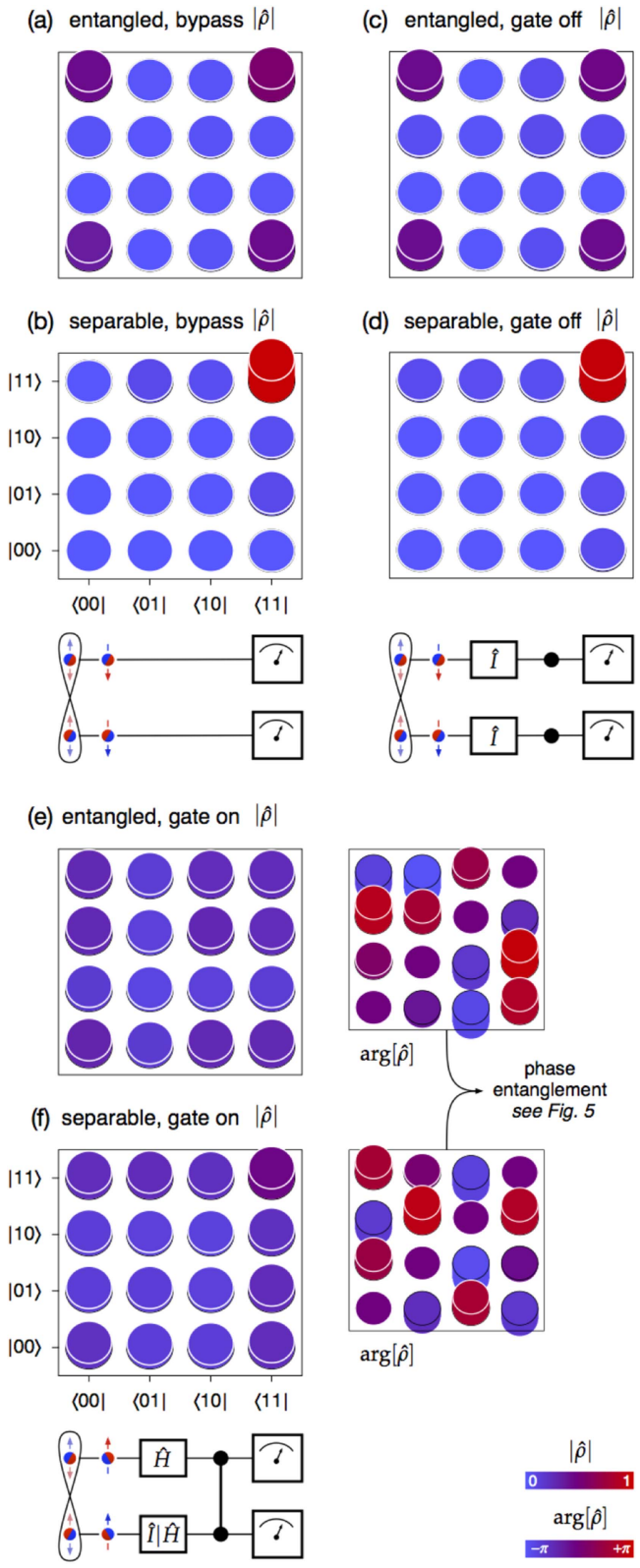

Figure 4. Reconstructed output states for various source and gate configurations. States (a), (c), (e) are seeded by an entangled source state, while (b), (d), (f) are seeded by a $|11\rangle$ source state. States (a), (b) bypass the gate; (c), (d) pass through the gate set to $\hat{I}$; and (e), (f) pass through the gate set to $\hat{cz}$, and include the phase information, below. State properties are compiled in table 1. Device configurations producing each set of states are shown at right.

In the non-degenerate SFWM process used here, two photons from a bright pump are annihilated, producing two correlated photons with different wavelengths (figure 1(a)). The two generated photons, 'signal' and 'idler', emerge spectrally on either side of the pump, conserving energy and momentum. In our experiment, spiralled 21 mm long waveguides were used to produce photon-pairs, with the pump, signal, and idler photon wavelengths being 1551, 1547 and 1555 nm. These photons were generated in a continuous spectrum and the chosen wavelengths were post-selected by the off-chip demultiplexers.

2.2. Entangled qubits generation

Our device uses a new scheme to generate entangled path-encoded states, which can subsequently be interfered, using pairs of *non-degenerate* photons. Pump laser is distributed between two reverse-HOM structures using a reconfigurable power splitter (splitting ratio $\sin^2[\phi_\beta/2]$). Each RHOM contains two spiralled waveguides and a thermal phase shifter, as in [28]. The internal RHOM phases (ϕ_T and ϕ_B) were set to $\pi/2$, such that the produced photon-pairs emerged deterministically split, one in each output waveguide, and in a state symmetrical between signal and idler photons. ϕ_β allows us to control the balance of photon-pair emission between the two RHOM structures, and so to control the entanglement present in the two-qubit output state.

Following figure 1(b), if $\phi_\beta = \pi$, photons will be generated only in the top RHOM, and the photon number output state, after the waveguide crossing, will be $|1010\rangle$, or $|00\rangle$ in the qubit basis. On the other hand, if $\phi_\beta = 0$, only the bottom RHOM generates photons, leading to $|0101\rangle = |11\rangle$. Finally, if $\phi_\beta = \pi/2$, we obtain the maximally entangled state: $|\Phi^\Theta\rangle \equiv (|00\rangle + e^{i\Theta}|11\rangle)/\sqrt{2}$, where Θ is a fixed phase factor due to the chip's intrinsic path-length mismatch. Thus, the output state from the entangled qubit generator is

$$|\psi\rangle = \sqrt{\beta}|00\rangle + e^{i\Theta}\sqrt{1-\beta}|11\rangle \qquad (1)$$

which can be continuously varied across a wide range of separable and entangled states, depending on the balance parameter, β. The balance depends on the square of the power division of the state control Mach–Zehnder interferometers (MZI) (controlled by the phase ϕ_β), due to the two-photon dependence of SFWM:

$$\beta = \left| \frac{\sin^2(\phi_\beta/2)}{\sqrt{\sin^4(\phi_\beta/2) + \cos^4(\phi_\beta/2)}} \right|^2 . \qquad (2)$$

2.3. Quantum logic and analysis

The state $|\psi\rangle$ is fed into a two-qubit circuit, composed of single-qubit rotations, and a switchable entangling gate. We implemented the arbitrary rotations on each qubit by cascading phase-shifters and MZI. These were used to realise $\hat{R}_z$ and $\hat{R}_y$ rotations, respectively, obtaining an arbitrary SU(2) with the combination $\hat{R}_z \cdot \hat{R}_y \cdot \hat{R}_z$.

Table 1. Purity, Schmidt number, CHSH parameters and fidelity for a variety of measured states. The Schmidt number and CHSH parameter indicate entanglement. $S > 2$ indicates the presence of non-local correlations [42], while K indicates the number of coefficients in the Schmidt decomposition of the state [43]. The fidelities F' reported are computed against the ideal state optimised over local R_z rotations, to compensate for the intrinsic random phase factor on each qubit.

Source state	Gate	Purity P	Schmidt number K	CHSH S	Fidelity F'
$\|00\rangle$	Bypassed	0.995 ± 0.012	1.012 ± 0.011	1.577 ± 0.072	0.973 ± 0.011
$\|00\rangle$	$\hat{I}$	0.946 ± 0.031	1.034 ± 0.017	1.465 ± 0.064	0.962 ± 0.016
$\|11\rangle$	Bypassed	0.998 ± 0.008	1.004 ± 0.006	1.511 ± 0.049	0.984 ± 0.007
$\|11\rangle$	$\hat{I}$	0.949 ± 0.055	1.048 ± 0.037	1.601 ± 0.121	0.948 ± 0.031
$(\|00\rangle + \|11\rangle)/\sqrt{2}$	Bypassed	0.864 ± 0.019	1.905 ± 0.022	2.560 ± 0.037	0.909 ± 0.028
$(\|00\rangle + \|11\rangle)/\sqrt{2}$	$\hat{I}$	0.832 ± 0.040	1.936 ± 0.025	2.538 ± 0.072	0.900 ± 0.026
$\|++\rangle$	$\hat{cz}$	0.931 ± 0.036	1.657 ± 0.045	2.560 ± 0.078	0.873 ± 0.038
$(\|00\rangle + \|11\rangle)/\sqrt{2}$	$\hat{cz}$	0.900 ± 0.071	1.166 ± 0.055	1.907 ± 0.137	0.839 ± 0.013

We implemented a switchable entangling gate using a scheme based on [44], but replacing the $1/3$ beam-splitters with tunable-reflectivity MZIs. In this way, we can switch the gate's controlled-Z operation on and off. When on, the cz operation succeeds with probability $1/9$. In the remaining $8/9$ cases, non-qubit states are generated, which are filtered by the coincidence-counting post-selection. Note that only the on $(\cos(\theta_{cz}) = 1/3)$ and off $(\cos(\theta_{cz}) = -1)$ gate configurations produce unitary operations. The two qubit gate is followed by rotations (parametrised by θ_{Mz3}, θ_{My2}, $M \in \{T, B\}$) used to implement quantum state tomography, via the method described in [48].

2.4. Calibration

Since the phase shifter parameters (phase-per-electrical-power, and phase offset) varied between phase modulators, a calibration process was essential. Measuring the bright-light transmission from the inputs (IN and IN′) to the outputs (OUT_T, OUT_B, OUT'_T, OUT'_B), we were able to characterise the electro-optic parameters of each thermal phase shifter, in a similar way to that described in [49]. We learned the parameters associated with each phase according to the scheme:

$$\begin{aligned}
&\mathrm{IN}' \rightarrow \mathrm{OUT}'_T, \mathrm{OUT}'_B : \phi_B, \theta_{By1}, \theta_{\mathrm{CZB}}, \theta_{Ty1}, \theta_{\mathrm{CZT}}\\
&\mathrm{IN} \rightarrow \mathrm{OUT}'_T, \mathrm{OUT}'_B : \phi_\beta, \phi_T, \theta_{Tz1}, \theta_{Bz1}\\
&\mathrm{IN} \rightarrow \mathrm{OUT}_T : \theta_{\mathrm{CZC}}, \theta_{Ty2}, \theta_{Tz2}, \theta_{Tz3}\\
&\mathrm{IN} \rightarrow \mathrm{OUT}_B : \theta_{By2}, \theta_{Bz2}, \theta_{Bz3}.
\end{aligned} \tag{3}$$

We observed instabilities in the calibration data, due to changes in electrical contact resistance between our probe card and the on-chip gold pads. To mitigate this, we periodically recalibrated the on-chip parameters. Metallurgical wire-bonded contacts can prevent this in future. Low levels of thermal and common-ground crosstalk were observed but not compensated. Recent results suggest that crosstalk can be reduced through efficiency improvements, passive compensation methods, and by current driving of the thermal phase shifters [38, 49, 50].

The offsets of the tomographic z-rotation phases (θ_{Tz3}, θ_{Bz3}) were left at zero, meaning that additional random (fixed) z rotations were applied to each qubit before measurement. This choice was necessitated by the combined difficulty of: (1) calibrating the nonlinear source phase with bright light, and (2) doing this for each setting of the gate, in the device's finite stability time.

3. Results

3.1. Source performance

One of the key metrics of a photon-pair source is its pair-generation efficiency [51]. This quantity is obtained from the photon-pair detection rate as a function of the input power, accounting for loss and detector efficiency. Inside the 1 nm wide signal and idler spectral bands, we measured a brightness of 20 kHz mW^{-2}.

The indistinguishability between photon-pair sources is also important. The contrast of the RHOM block's quantum interference fringes indicates the indistinguishability of the block's constituent photon-pair sources. We measured RHOM quantum interference fringes on each source by configuring the chip to maximise photon flux at the OUT'_T and OUT'_B outputs, then varying ϕ_T and ϕ_B to obtain the fringes of figure 2. We pumped the bottom source via the auxiliary input IN′, and the top source via IN and the state-control MZI, integrating each point for 5 s. We observed $C = 93.2\% \pm 1.4\%$ and $72.9\% \pm 0.8\%$ fringe contrasts, respectively, for the top and bottom sources. Here, $C = (N_{\max} - N_{\min})/(N_{\max} + N_{\min})$, where $N_{\max}$ and $N_{\min}$ are the accidental-subtracted maximum and minimum fitted count rates. The reduced contrasts can be explained by deviations (from the ideal $\eta = 50\%$) in the input evanescent couplers of each RHOM structure; they are compatible with reflectivity values of $\eta \approx 43\%$ and $\eta \approx 36\%$ for the top and bottom sources, respectively.

3.2. Quantum logic

We next quantified the device's control over entanglement. Quantum state tomography was used to extract the purity ($P = \mathrm{Tr}(\hat{\rho}^2)$ [41]), the CHSH parameter, a strict measurement of quantum correlations, and the Schmidt number, analogous to the number of pure states represented in a given density

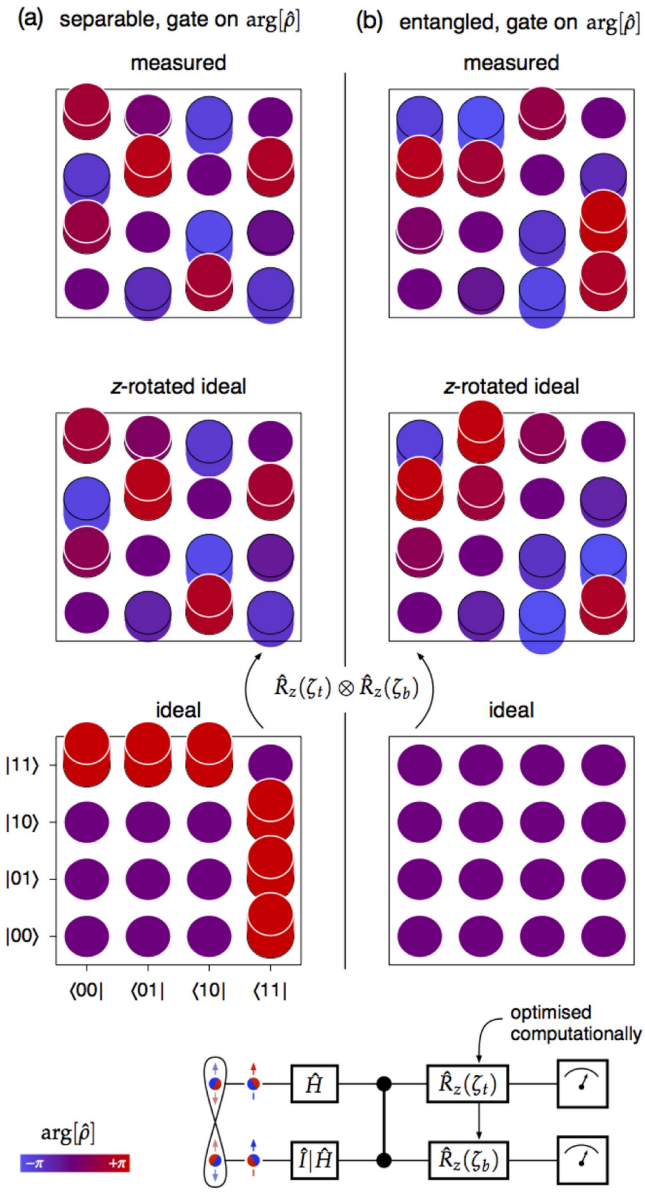

Figure 5. Detail of phase entanglement, separability of states shown in figures 4(e) and (f). Since the cz gate operates on phase, random, fixed, local z-rotations obscure the underlying performance. The connection between the measured and ideal states, via numerical optimisation of ζ_t and ζ_b, is shown for (a) the gate-entangled, and (b) gate-disentangled states. In both cases, the ideal density matrix magnitude is constant, $|\hat{\rho}_{i,j}| = 1/4$.

matrix. These last two metrics show how separable the state is. The CHSH inequality, $S(\hat{\rho}) \leqslant 2$ [31, 42, 52], is violated when the state $\hat{\rho}$ cannot be represented by a local classical theory, indicating its entangled quantum nature. The Schmidt number, on the other hand, is an entanglement monotone and can give further evidence of the entangled or separable nature of $\hat{\rho}$ [42, 43, 53]. CHSH parameter values were obtained by computationally selecting an optimal measurement set for each of the states under analysis [31].

We analysed a wide set of separable and entangled quantum states produced by the two-qubit source. Fixing $\phi_T = \phi_B = \pi/2$, we varied the phase of the state control MZI, ϕ_β, between 0 and π to prepare variably entangled states in the form of (1). When $\beta = 0$ or 1, separable states result, while when $\beta = 1/2$, a maximally entangled state is produced. States obtained directly from the source (bypassing the gate) showed good agreement with (1). These were measured using the $\mathrm{OUT}_T{}'$ and $\mathrm{OUT}_B{}'$ auxiliary outputs (see figure 1(b)). Measured and calculated variations of the balance, Schmidt number, and CHSH parameter are plotted in figure 3, versus the state control parameter ϕ_β.

In figure 4 we show a sample of density matrices arising from the main device configurations, and we list their properties (purity, Schmidt number, CHSH parameter, and fidelity with the ideal z-rotated state) in table 1. Errors were obtained from Monte-Carlo simulations, based on 200 samples of Poissonian photon noise and accompanying tomographic reconstructions [54]. As expected, the $\hat{I}$-mode gate did not substantially affect the properties of the input states. The $\hat{c}\hat{z}$-mode gate, however, acted to entangle separable states, and separate entangled states, though it also degraded the purity. The limited contrast in the quantum interference of the two RHOM sources contributed to this reduction, by occasionally depositing two photons into one 'qubit'. Gate and tomography calibration errors likely also contributed.

Since the entangling gate operates on the input state's *phase*, we must examine with care the phase of the output state, $\arg[\hat{\rho}]$. The intrinsic and uncalibrated z-rotations on each qubit result in complicated phase pictures (figures 4(e) and (f)). To compare these to their ideal counterparts, we computationally applied $\hat{R}_z(\zeta_t) \otimes \hat{R}_z(\zeta_b)$ to the reconstructed output state, and optimised the fidelity over local z-rotations via ζ_t and ζ_b. The resulting fidelities are listed in table 1 and the process is shown visually in figure 5.

4. Discussion

We have presented a silicon-on-insulator quantum photonic device which embeds capabilities for the generation, manipulation, and analysis of two-qubit entangled states, by leveraging on-chip linear and nonlinear optics. We showed how the device can prepare a variety of entangled and separable states, and operate on them using a switchable entangling gate. We demonstrated a new reconfigurable source of variably path-entangled non-degenerate photon pairs, using RHOM quantum interference, and used on-chip quantum state tomography to measure its performance. The integration of this source with a complex integrated linear optical network enabled both the entanglement and disentanglement of the on-chip generated quantum states.

Device performance was hindered by imperfect beamsplitters and high coupling losses, leading to issues with stability, and ultimately limiting the measurable purity and entanglement. However, the use of more advanced fibre couplers, such as those based on ultra-low loss gratings [55], together with adaptive methods, employing multiple imperfect MZIs for the realisation of a very high-quality one [34], can overcome these limitations, and enable high-performance,

large-scale silicon photonic quantum devices in the near future.

Acknowledgments

We thank Damien Bonneau, Jianwei Wang, and Dylan Mahler for valuable discussions and support. We are grateful to Alasdair Price for help with preliminary characterisation. We also thank the staff of the James Watt Nano-fabrication Centre in Glasgow. We acknowledge support from the European Union through the BBOI, and from the QUCHIP projects. R H Hadfield, J L O'Brien and M G Thompson acknowledge support from the Engineering and Physical Sciences Research Council (EPSRC, UK) (Grant numbers EP/L024020/1 and EP/K033085/1). M G Thompson acknowledges support from the European Research Council (ERC Grant Agreement number: 640079 QPE ERC-2014-ST). J W Silverstone acknowledges an EPSRC Doctoral Training Account, and a Natural Sciences and Engineering Research Council (Canada) Alexander Graham Bell Canada Graduate Scholarship. J L O'Brien acknowledges a Royal Society Wolfson Merit Award and a Royal Academy of Engineering Chair in Emerging Technologies.

Author contributions statement

RS and JWS contributed equally to this work. They conceived and designed the device, performed the experiments, and analysed the data. MJS and M Sorel. fabricated the device. SM, TY, MF, M Sasaki, and HT provided the superconducting detectors and M G Tanner, CMN, and RHH built the detector system. M G Thompson supervised the work. All authors contributed to the manuscript.

Data availability

The data that support the plots within the paper and other findings of the study are available from the open data repository Figshare in https://doi.org/10.6084/m9.figshare.5464381.v1.

ORCID iDs

R Santagati https://orcid.org/0000-0001-9645-0580
J W Silverstone https://orcid.org/0000-0002-3429-4890
M Sasaki https://orcid.org/0000-0002-9508-570X

References

[1] O'Brien J L, Furusawa A and Vuckovic J 2009 Photonic quantum technologies *Nat. Photon.* **3** 687–95
[2] Latmiral L, Spagnolo N and Sciarrino F 2016 Towards quantum supremacy with lossy scattershot boson sampling *New J. Phys.* **18** 113008
[3] Politi A, Cryan M J, Rarity J G, Yu S and O'Brien J L 2008 Silica-on-silicon waveguide quantum circuits *Science* **320** 646–9
[4] Metcalf B J *et al* 2014 Quantum teleportation on a photonic chip *Nat. Photon.* **8** 770–4
[5] Minkov M and Savona V 2016 A compact, integrated silicon device for the generation of spectrally filtered, pair-correlated photons *J. Opt.* **18** 054012
[6] Matsuda N *et al* 2014 On-chip generation and demultiplexing of quantum correlated photons using a silicon-silica monolithic photonic integration platform *Opt. Express* **22** 22831–40
[7] Reimer C *et al* 2015 Cross-polarized photon-pair generation and bi-chromatically pumped optical parametric oscillation on a chip *Nat. Commun.* **6** 9236
[8] Carolan J *et al* 2015 Universal linear optics *Science* **349** 711–6
[9] Sansoni L *et al* 2010 Polarization entangled state measurement on a chip *Phys. Rev. Lett.* **105** 200503
[10] Tillmann M *et al* 2013 Experimental boson sampling *Nat. Photon.* **7** 540–4
[11] Flamini F *et al* 2015 Thermally reconfigurable quantum photonic circuits at telecom wavelength by femtosecond laser micromachining *Light Sci. Appl.* **4** 354
[12] Bentivegna M *et al* 2015 Experimental scattershot boson sampling *Sci. Adv.* **1** 1400255
[13] Spring J B *et al* 2017 Chip-based array of near-identical, pure, heralded single-photon sources *Optica* **4** 90–6
[14] Vergyris P *et al* 2016 On-chip generation of heralded photon-number states *Sci. Rep.* **6** 1500
[15] Alibart O *et al* 2016 Quantum photonics at telecom wavelengths based on lithium niobate waveguides *J. Opt.* **18** 104001
[16] Lenzini F *et al* 2017 Active demultiplexing of single photons from a solid-state source *Laser Photon. Rev.* **11** 1600297
[17] Sansoni L *et al* 2017 A two-channel, spectrally degenerate polarization entangled source on chip *npj Quantum Inf.* **3** 5
[18] Zhang X, Zhang Y, Xiong C and Eggleton B J 2016 Correlated photon pair generation in low-loss double-stripe silicon nitride waveguides *J. Opt.* **18** 074016
[19] Moss D J, Morandotti R, Gaeta A L and Lipson M 2013 New CMOS-compatible platforms based on silicon nitride and Hydex for nonlinear optics *Nat. Photon.* **7** 597–607
[20] Silverstone J W, Bonneau D, O'Brien J L and Thompson M G 2016 Silicon quantum photonics *IEEE J. Sel. Top. Quantum Electron.* **22** 6700113
[21] Sharping J E *et al* 2006 Generation of correlated photons in nanoscale silicon waveguides *Opt. Express* **14** 12388–93
[22] Azzini S *et al* 2012 Ultra-low power generation of twin photons in a compact silicon ring resonator *Opt. Express* **20** 23100–7
[23] Matsuda N *et al* 2012 A monolithically integrated polarization entangled photon pair source on a silicon chip *Sci. Rep.* **2** 00817
[24] Olislager L *et al* 2013 Silicon-on-insulator integrated source of polarization-entangled photons *Opt. Lett.* **38** 1960–2
[25] Collins M J *et al* 2013 Integrated spatial multiplexing of heralded single-photon sources *Nat. Commun.* **4** 2582
[26] Xiong C *et al* 2016 Active temporal multiplexing of indistinguishable heralded single photons *Nat. Commun.* **7** 10853
[27] Harada K *et al* 2011 Indistinguishable photon pair generation using two independent silicon wire waveguides *New J. Phys.* **13** 065005
[28] Silverstone J W *et al* 2013 On-chip quantum interference between silicon photon-pair sources *Nat. Photon.* **8** 104–8

[29] Takesue H, Matsuda N, Kuramochi E and Notomi M 2014 Entangled photons from on-chip slow light *Sci. Rep.* **4** 448
[30] Xu X *et al* 2013 Near-infrared Hong–Ou–Mandel interference on a silicon quantum photonic chip *Opt. Express* **21** 5014–24
[31] Silverstone J W *et al* 2015 Qubit entanglement between ring-resonator photon-pair sources on a silicon chip *Nat. Commun.* **6** 7948
[32] Harris N C *et al* 2014 Integrated source of spectrally filtered correlated photons for large-scale quantum photonic systems *Phys. Rev.* X **4** 041047
[33] Piekarek M, Bonneau D, Miki S and Yamashita T 2016 High-extinction ratio integrated photonic filters for silicon quantum photonics *Opt. Lett.* **42** 815
[34] Wilkes C M *et al* 2016 60 dB high-extinction auto-configured Mach–Zehnder interferometer *Opt. Lett.* **41** 5318–21
[35] Najafi F *et al* 2015 On-chip detection of non-classical light by scalable integration of single-photon detectors *Nat. Commun.* **6** 5873
[36] Pernice W H P *et al* 2012 High-speed and high-efficiency travelling wave single-photon detectors embedded in nanophotonic circuits *Nat. Commun.* **3** 1325
[37] Xu Q, Fattal D and Beausoleil R G 2008 Silicon microring resonators with 1.5 μm radius *Opt. Express* **16** 4309
[38] Harris N C *et al* 2014 Efficient, compact and low loss thermo-optic phase shifter in silicon *Opt. Express* **22** 10487–93
[39] Shadbolt P J *et al* 2012 Generating, manipulating and measuring entanglement and mixture with a reconfigurable photonic circuit *Nat. Photon.* **6** 45–9
[40] Chen J, Lee K F and Kumar P 2007 Deterministic quantum splitter based on time-reversed Hong–Ou–Mandel interference *Phys. Rev.* A **76** 031804
[41] Gamel O and James D F V 2012 Measures of quantum state purity and classical degree of polarization *Phys. Rev.* A **86** 033830
[42] Horodecki R, Horodecki M and Horodecki K 2009 Quantum entanglement *Rev. Mod. Phys.* **81** 865–942
[43] Terhal B M and Horodecki P 2000 Schmidt number for density matrices *Phys. Rev.* A **61** 040301
[44] Ralph T, Langford N K, Bell T B and White A G 2002 Linear optical controlled-NOT gate in the coincidence basis *Phys. Rev.* A **65** 062324
[45] Trinh P D, Yegnanarayanan S and Jalali B 1995 Integrated optical directional couplers in silicon-on-insulator *Electron. Lett.* **31** 2097–8
[46] Miki S, Yamashita T, Terai H and Wang Z 2013 High performance fiber-coupled NbTiN superconducting nanowire single photon detectors with Gifford-McMahon cryocooler *Opt. Express* **21** 10208–14
[47] Leuthold J, Koos C and Freude W 2010 Nonlinear silicon photonics *Nat. Photon.* **4** 535–44
[48] James D F V, Kwiat P G, Munro W J and White A G 2001 Measurement of qubits *Phys. Rev.* A **64** 052312
[49] Santagati R *et al* 2016 Witnessing eigenstates for quantum simulation of Hamiltonian spectra arXiv:1611.03511
[50] Paesani S *et al* 2017 Experimental Bayesian quantum phase estimation on a silicon photonic chip *Phys. Rev. Lett.* **118** 100503
[51] Savanier M, Kumar R and Mookherjea S 2016 Photon pair generation from compact silicon microring resonators using microwatt-level pump powers *Opt. Express* **24** 3313–28
[52] Aspect A, Grangier P and Roger G 1982 Experimental realization of Einstein–Podolsky–Rosen–Bohm gedankenexperiment: a new violation of Bell's inequalities *Phys. Rev. Lett.* **49** 91–4
[53] Sperling J and Vogel W 2011 The Schmidt number as a universal entanglement measure *Phys. Scr.* **83** 045002
[54] Roos C F *et al* 2004 Bell states of atoms with ultralong lifetimes and their tomographic state analysis *Phys. Rev. Lett.* **92** 220402
[55] Ding Y, Ou H and Peucheret C 2013 Ultrahigh-efficiency apodized grating coupler using fully etched photonic crystals *Opt. Lett.* **38** 2732–4